Earth and Planetary Science Letters 429 (2015) 101–109

Contents lists available at ScienceDirect

Earth and Planetary Science Letters

www.elsevier.com/locate/epsl

Robust constraints on average radial lower mantle anisotropy and consequences for composition and texture

R.W.L. de Wit *, J. Trampert

Department of Earth Sciences, Utrecht University, Budapestlaan 4, 3584 CD, Utrecht, The Netherlands

ARTICLE INFO

Article history:
Received 26 February 2015
Received in revised form 20 July 2015
Accepted 26 July 2015
Available online 13 August 2015
Editor: J. Brodholt

Keywords:
mantle anisotropy
radial Earth structure
normal modes
uncertainty estimation
thermochemical structure

ABSTRACT

Seismic anisotropy has been observed in the upper mantle (<660 km depth) and the lowermost ~150–250 km of the mantle (the D″ region), while the remainder of the lower mantle is believed to be isotropic. Here, we used centre frequencies for spheroidal and toroidal normal modes together with a neural-network-based technique to infer probability density functions for the average radial anisotropy in the lower mantle. We show, for the first time, a robust observation that the average lower mantle is anisotropic (mainly in the parameter η) below 1900 km depth, challenging the consensus that this part of the mantle is isotropic. The mass density also shows a well-constrained positive deviation from existing models at the same depths. Using existing mineral physics data, our results are compatible with an average lower mantle that is about 100–200 K colder than commonly-assumed adiabats and that consists of a mixture of about 60–65% perovskite and 35–40% ferropericlase containing 10–15% iron. If further a crystal alignment mechanism is assumed, the observed anisotropy can constrain the orientation of the two minerals and suggests a new window to study the nature of flow in the lower mantle.

© 2015 Elsevier B.V. All rights reserved.

1. Introduction

Seismic anisotropy, the direction-dependence of elastic wave propagation, can be a key indicator of mantle flow, deformation and consequently mantle dynamics (Montagner, 1994; McNamara et al., 2002; Panning and Romanowicz, 2004). It is commonly interpreted as lattice-preferred orientation (LPO) or shape-preferred orientation (SPO) of the mineral crystals that constitute the mantle (Karato, 2008; Fichtner et al., 2013). LPO refers to the alignment of intrinsically anisotropic minerals, such as olivine, while SPO relates to (long-wavelength) apparent anisotropy that is observed as a result of a specific configuration of isotropic material, e.g. a stack of thin alternating layers with contrasting elastic properties, melts or cracks (Backus, 1962).

Seismic anisotropy has been observed in the upper mantle (above the 660 km discontinuity) and the lowermost ~150–250 km of the mantle (Montagner and Kennett, 1996; Panning and Romanowicz, 2004; Beghein et al., 2006; Visser et al., 2008; Chang et al., 2014). By contrast, the current consensus is that the remainder of the lower mantle is isotropic, although both experimental and modelling studies have shown that lower mantle minerals are intrinsically anisotropic (Meade et al., 1995; Mainprice et al., 2000). Karato et al. (1995) explained the absence of lower mantle anisotropy by super-plastic flow, since the associated diffusion creep does not lead to the development of LPO of mantle minerals. There are also no viable candidates known for SPO in the lower mantle.

Most seismically anisotropic earth models suffer from several limitations. Firstly, there is a well-documented trade-off between anisotropy in the crust and in the mantle (Bozdağ and Trampert, 2008; Panning et al., 2010). Secondly, seismological inverse problems are notoriously non-unique. Thirdly, a certain scaling is often imposed between chosen model parameters to simplify the seismological inverse problem and reduce the number of free parameters, which may lead to biased models (Beghein et al., 2006; Panning and Romanowicz, 2006; Kustowski et al., 2008). Finally, regularisation is commonly applied to stabilise the inverse problem, which can have a significant effect on the final solution (Beghein and Trampert, 2003; de Wit et al., 2012). These issues call for a quantitative assessment of model uncertainties. Nonetheless, most models come without error bars, which makes it impossible to quantify the discrepancies between existing models.

We assessed anisotropy in the lower mantle (>660 km depth) in a fully quantitative manner, i.e. we solved the inverse problem and estimated uncertainties without imposing any scaling between parameters. We adopted a Bayesian framework, in which any inference made about a model is the result of the conjunction of our current (*prior*) knowledge and the ability of the model to explain

* Corresponding author. Tel.: +31 (0)30 253 5135.
E-mail address: ralphdewit@gmail.com (R.W.L. de Wit).

http://dx.doi.org/10.1016/j.epsl.2015.07.057
0012-821X/© 2015 Elsevier B.V. All rights reserved.

the observations (Tarantola and Valette, 1982). The updated (*posterior*) knowledge on the model — that is, after observing the data — represents the new degree of belief in the model, expressed by a probability density function (pdf). We only consider the marginal posterior pdfs for single earth model parameters, averaged over a certain depth range. Such a 1-D marginal posterior pdf, hereafter referred to as 'marginal', represents the information on a single model parameter, given the data and the possible variations in all other model parameters. We employed machine learning techniques to learn relationships between data and model based on samples of the prior model space. To obtain marginals, we used a Mixture Density Network (MDN, Bishop, 1995; de Wit et al., 2013; Käufl et al., 2014), which takes the seismic data as input and outputs the marginal for the earth model parameter of interest. Our inversion method is designed to provide a flexible tool for hypothesis testing, which allows us to assess the probability of a certain statement or hypothesis. The flexibility enables us to focus on averages of any parameter of interest over an arbitrary depth range (de Wit et al., 2014), rather than focus on the parameters at a given depth, as used by the forward calculation, which are difficult to resolve by the data used. In this study, we used splitting function measurements for spheroidal (Deuss et al., 2013; Koelemeijer et al., 2013; Koelemeijer, 2014) and toroidal (Reference Earth Model, 2001) modes. We focus here on the radial (1-D) seismic structure of the lower mantle and show that this region is indeed anisotropic.

Firstly, we briefly describe the earth model parametrisation, the neural network methodology and the normal mode data. Secondly, we 'invert' the centre frequency measurements using MDNs and construct 1-D marginal posterior pdfs for the radial averages of P-wave (V_P) and S-wave (V_S) velocities, density (ρ) and three parameters describing radial anisotropy in six layers in the lower mantle. Finally, we assess whether the observed elasticity, as represented by the 1-D marginals for the seismic parameters in each layer, can be explained by a simple thermochemical lower mantle model, given currently available mineral physics data.

2. Model parametrisation

The radial structure of the Earth is parametrised in terms of wavespeeds, density and bulk and shear attenuation ($1/Q_\kappa$ and $1/Q_\mu$, respectively). We allowed for radial anisotropy in the whole mantle and inner core, while the outer core was isotropic. The radial anisotropy was parametrised by the velocities of vertically and horizontally propagating P-waves (V_{PV} and V_{PH}), the velocities of vertically and horizontally polarised S-waves propagating horizontally (V_{SV} and V_{SH}) and the fifth anisotropic parameter η, similar to the parametrisation of the Preliminary Reference Earth Model (*PREM*, Dziewoński and Anderson, 1981). We used a finely layered parametrisation with depth on a discrete set of 185 points (similar to the models used in the Mineos package Masters et al., 2011) and allowed the depths of the discontinuities to vary. No correlations between physical parameters were imposed, i.e. velocity, density ρ, η and attenuation profiles were constructed independently from each other. We introduced correlations between adjacent depth points, based on randomly perturbed *PREM*-gradients, to exclude physically implausible models and restrict the size of the model space. In addition, similar to *PREM*, we imposed constraints on the mass and moment of inertia of the earth models (Chambat and Valette, 2001).

We generated 100 000 synthetic models, which were randomly drawn from the prior model distribution. The prior for the velocities, density and anisotropic parameters was centred on *PREM*, but spans a wide range of values (Supplementary Figure A.1). In general, wave velocities, density and η were allowed to vary with respect to *PREM* by ±5% in the upper mantle and ±3% in the lower mantle and core. The prior ranges for discontinuity depths included deviations from *PREM* of several tens of kilometres and the prior for attenuation parameters spanned multiple orders of magnitude. The exact prior ranges for all earth model parameters and further details on the parametrisation and the implementation of the correlation between depths points can be found in de Wit et al. (2014).

A radially anisotropic medium can be described by hexagonal symmetry with a vertical (radial) symmetry axis, density and the five independent Love coefficients A, C, N, L and F (Love, 1927). Three parameters are commonly used to describe the radial anisotropy: the P-wave anisotropy ($\phi = \frac{C}{A} = \frac{V_{PV}^2}{V_{PH}^2}$), the shear-wave anisotropy ($\xi = \frac{N}{L} = \frac{V_{SH}^2}{V_{SV}^2}$) and $\eta = \frac{F}{A-2L}$, which corresponds to anisotropy at intermediate incidence angles. In addition to the three anisotropic parameters, we studied the density and the isotropic equivalents of the P- and S-wave velocities, which are given by the Voigt averages (Babuska and Cara, 1991; Panning and Romanowicz, 2006),

$$V_P = \sqrt{\frac{K + \frac{4}{3}G}{\rho}} \tag{1}$$

and

$$V_S = \sqrt{\frac{G}{\rho}}, \tag{2}$$

where the Voigt average bulk and shear moduli, K and G respectively, are defined as

$$K = (C + 4A - 4N + 4F)/9 \tag{3}$$

and

$$G = (C + A + 6L + 5N - 2F)/15. \tag{4}$$

with the five independent Love coefficients A, C, N, L and F. We note that our results are not affected by the choice between a parametrisation in terms of the Love coefficients or wave velocities and η, as our method is derivative-free. It is straightforward to extract the five Love coefficients from the polarised wave velocities and η in an earth model and calculate the corresponding ϕ, ξ and Voigt average isotropic wave velocities (Equations (1)–(4)).

Rather than focusing on the individual depth points of the original earth model parametrisation, which we could not resolve with the data used, we estimated the radially averaged η, ϕ, ξ, ρ and the Voigt average equivalent isotropic V_P and V_S in six lower mantle layers. The bulk of the lower mantle was divided into five layers of roughly equal thickness, which had approximate depth ranges 670–1027, 1027–1456, 1456–1884, 1884–2313 and 2313–2741 in kilometres. The sixth and deepest layer (2741–2891 km) represents the D″ region, which is well-known to be anisotropic (see Nowacki et al., 2011; Chang et al., 2014 for reviews). Note that the depths of the three discontinuities enclosing the lower mantle and the D″ region, i.e. the top of the lower mantle (670 km), the top of the D″ region (2741 km) and the core–mantle boundary (CMB, 2891 km), were allowed to vary by ±20–30 km between the earth models (de Wit et al., 2014). For each model, the depths of the remaining boundaries of the five lower mantle layers were determined by linearly interpolating between the new depths of the discontinuities at 670 and 2741 km.

Note that all other parameters in the model, i.e. parameters describing bulk and shear attenuation, core and upper mantle structure, are also allowed to vary within our prior model distribution (Supplementary Figure A.1). We further emphasise that we did

not impose constant-value layers in the earth models used for the forward calculations. All synthetic data are based on model parameters varying on the 185 points of the original Mineos description with spline interpolation in between. The MDNs can be trained directly on the radially averaged structure in an arbitrary layer, while the underlying 1-D earth models in the training set are physically realistic, i.e. smooth, similar to existing reference models. In other words, we chose to study the constraint offered by the data on the average values across the six layers defined above, instead of the value at a specific depth. As such, our approach is comparable to a Backus–Gilbert averaging technique, but now with predefined kernels (Backus and Gilbert, 1968, 1970).

3. Methodology

In the Bayesian framework, any inference made about a model is the result of the conjunction of our current (*prior*) knowledge and the ability of the model to explain the observations (Tarantola and Valette, 1982). We used artificial neural networks to solve a Bayesian inverse problem. Neural networks are very common in pattern recognition problems, such as image or speech recognition, and can approximate an arbitrary non-linear function, using a set of synthetic examples of corresponding input-output pairs (Bishop, 1995). These samples are presented to a network in a so-called *training* process, during which the free parameters of a network were modified to approximate the function of interest. In our case, the function of interest is the inverse mapping from seismic data to earth model parameters. Once successfully trained, the neural network can be applied to the seismic data and make a prediction for the values of model parameters. The particular class of neural network we used here, the Mixture Density Network (MDN), takes the seismic data as input and outputs the marginal posterior pdf for the parameter(s) of interest (Bishop, 1995; Meier et al., 2007; de Wit et al., 2013). Our method is flexible, as we are free to choose the output, or *target*, parameter for the MDN. This allows us to ask specific questions, i.e. test hypotheses, about an arbitrary (combination of) model parameter(s), such as the depth of a seismic discontinuity or the average shear-wave anisotropy in a mantle layer of arbitrary thickness.

In this study, we only consider 1-D targets and thus focus on 1-D marginal posterior pdfs, or "marginals". Marginal pdfs can be used to test hypotheses on individual model parameters, i.e. allow us to answer specific questions. They reflect our knowledge of a single model parameter, given the data and arbitrary values for all other model parameters, e.g. Tarantola (2005). Naturally, 1-D marginals do not contain information on higher-dimensional structures in the posterior model space, such as trade-offs between the parameters. Such information is available in the full posterior model distribution or in higher-order ($\geq$2-D) marginals, which we can also calculate (de Wit et al., 2014).

Neural network training is sensitive to the random initialisation of the network parameters. To minimise this sensitivity, we trained several neural networks with different initialisations, and subsequently combined these networks in an ensemble, or committee, of networks. A network ensemble can result in better generalisation, i.e. achieve a better prediction accuracy on unseen data (Bishop, 1995). The ensemble output was formed by a weighted average of the members, where the individual weights were determined by each network's performance on the same test set (Käufl et al., 2014; de Wit et al., 2014).

We considered a total of 36 1-D target parameters (the radial averages of six seismic parameters in six lower mantle layers). For each target parameter, we constructed an ensemble of 48 networks. The MDNs consisted of 50 hidden units and a mixture of 15 Gaussian kernels. The networks were trained using the Scaled Conjugate Gradient (SCG) algorithm (Møller, 1993) for a maximum of 5000 iterations. As in previous studies (de Wit et al., 2013, 2014), we employed early stopping, which means that network training is halted when the error of a separate validation set reaches a minimum. We used 80% of the 100 000 patterns in the synthetic data set for training and 15% for the validation set. The remaining 5% is allocated to a test set, but this test set is not used for individual networks. Only after training of all 48 networks, we use a single test set of 5000 patterns, randomly selected from the synthetic data set, to assess the performance of all 48 ensemble members and determine the relative weight of each member in the ensemble average (de Wit et al., 2014). For each network realisation, training and validation sets were randomly drawn from the synthetic data set to enhance the generalisation capability of the ensemble.

3.1. Information gain

For each target parameter, we calculated the information gain between the 1-D marginal posterior and prior pdfs, as quantified by the Kullback–Leibler divergence D_{KL} (MacKay, 2003). D_{KL} measures the information gained for a particular model parameter upon observing the data (de Wit et al., 2014; Käufl et al., 2014). If the data have no sensitivity to a region within the Earth, we will not learn anything from the data, i.e. we will not extract information that is not already available in the prior pdf. In such a case, the information gain $D_{KL} = 0$ and the MDN output will resemble the prior pdf. For reference, consider a 1-D Gaussian distribution with mean μ and standard deviation σ. The difference between this distribution and a second distribution with the same mean and standard deviation $\frac{1}{2}\sigma$, as measured by the information gain, is 1.16 bits.

4. Normal mode data

Normal mode theory provides a means to relate the Earth's free oscillations to Earth structural parameters (Dahlen and Tromp, 1998). Spheroidal and toroidal modes have a complementary sensitivity to P-SV and SH motion, respectively, and a joint inversion of these two types of free oscillations can provide a strong constraint on the anisotropic structure. Therefore, we used centre frequencies derived from self-coupled splitting function measurements for spheroidal and toroidal modes. Splitting function measurements naturally separate structure with radial symmetry from 3-D variations, e.g. Woodhouse and Giardini (1985). Centre frequencies only depend on the degree-zero splitting function coefficients c_{00} and are thus only sensitive to spherically symmetric or radial (1-D) Earth structure. We did not use splitting coefficients of higher degrees, since they correspond to lateral variations in Earth structure. Therefore, our data are only sensitive to radial anisotropy.

4.1. Spheroidal modes

Similar to de Wit et al. (2014), we used 184 self-coupled spheroidal mode centre frequencies up to 10 mHz, the majority of which were measured by Deuss et al. (2013) (Supplementary Figure A.2). This extensive recent catalogue contains new modes which are sensitive to V_P and inner core structure. We supplemented this catalogue with similar measurements for Stoneley modes (Koelemeijer et al., 2013), fundamental modes ${}_0S_{22}-{}_0S_{30}$ and ${}_2S_{17}$ (Koelemeijer, 2014). We also experimented with older spheroidal data from the Reference Earth Model (REM) web pages (http://igppweb.ucsd.edu/~gabi/rem.dir/surface/smodes.list).

4.2. Toroidal modes

We used "best estimate" mean frequencies for toroidal modes, as made available on the REM web pages (http://igppweb.ucsd.edu/~gabi/rem.dir/surface/tmodes.list). We selected toroidal modes with radial orders $n = 0$–5 and angular orders similar to those of the spheroidal modes, i.e. $l = 1$–30 (Supplementary Figure A.2). The resulting data set included 125 toroidal mode measurements with frequencies up to 8 mHz, almost half of which were measured by Widmer (1991). By adding the 125 toroidal modes to the 184 spheroidal mode measurements, we almost doubled the dimensionality of the input to the neural networks. Consequently, the training times for the neural network increased. A total of 287 toroidal mode measurements (for higher angular orders) is available on the REM website, but we decided to limit the number of toroidal modes to align the two data sets in terms of angular orders ($l = 1$–30). An obvious advantage is that the total input dimensionality ($184 + 125 = 309$) remains relatively low (compared to $184 + 287 = 471$), and so do the number of free network parameters, the required number of training samples and thus computation time. The neglected modes also have more sensitivity in the upper mantle.

4.3. Synthetic data

We used the Mineos package (Masters et al., 2011) to calculate exact normal mode frequencies for 100 000 synthetic 1-D earth models, which we generated randomly from the prior model distribution (Supplementary Figure A.1). Self-gravitation was taken into account for frequencies below 30 mHz and a reference period of 1 s was used for the dispersion correction due to attenuation. The synthetic data for the normal modes thus consisted of 309 ($184 + 125$) free oscillation centre frequencies. The synthetic data were corrupted by adding Gaussian noise with zero mean and a standard deviation given by the uncertainty estimate for each measurement, as reported by Deuss et al. (2013), Koelemeijer et al. (2013), Koelemeijer (2014) and on the REM website (http://igppweb.ucsd.edu/~gabi/rem.dir/surface/tmodes.list). We note that the measurement errors were estimated using a cross-validation approach, which may not fully account for any systematic uncertainties. Furthermore, *PREM* was used as a reference model in an iterative damped least-squares inversion of normal-mode spectra for splitting function coefficients, e.g. Deuss et al. (2013). As such, the coefficients could in principle be biased towards *PREM*. However, Deuss et al. (2013) note that the degree-zero coefficients c_{00}, from which the centre frequencies are derived, are the most robust parameters in their inversion, to which no damping is applied; therefore, the bias is assumed to be minimal.

5. Results

5.1. Inferences on lower mantle seismic structure

It is common practice to test the prediction accuracy of trained neural networks. Therefore, before analysing any marginal, we assess the MDNs with 5000 synthetic test samples, which were not used during the training process (results are not shown here, but examples can be found in de Wit et al. (2014)). Radial (1-D) seismological models, such as the Preliminary Reference Earth Model (*PREM*, Dziewoński and Anderson, 1981), are commonly used as a reference for 3-D tomographic models or to constrain the Earth's radial temperature and composition profiles (Kennett, 2006; Cobden et al., 2009; Cammarano et al., 2011). We also applied the trained MDNs to synthetic data corresponding to *PREM*, which were not used to train the networks. We found that the MDNs made accurate predictions for the test samples and for *PREM*, for which all parameters lay within one standard deviation of the most probable value in the marginals (Supplementary Figure A.3). The 1-σ performance provides evidence that the number of synthetic samples we use here (100 000) is sufficient to train the MDNs. We experimented with doubling the number of samples but found little change in the marginals. The width of the marginals reflects the trade-offs between the earth model parameters (examples can be found in de Wit et al., 2014) as well as the resolving power of the data, given data uncertainties.

Table 1
Probability of the anisotropy b in the average η, ϕ and ξ being negative, i.e. $p(b < 1)$, and stronger than -0.5%, i.e. $p(b < 0.995)$, for the five lower mantle layers and the D″ region. Note that the depths of discontinuities and the layer boundaries were allowed to vary between earth models (Section 2).

Region	Depth (km)	$p(b<1)$			$p(b<0.995)$		
		$\bar{\eta}$	$\bar{\phi}$	$\bar{\xi}$	$\bar{\eta}$	$\bar{\phi}$	$\bar{\xi}$
LM_I	670–1027	0.56	0.82	0.23	0.28	0.48	0.03
LM_{II}	1027–1456	0.22	0.87	0.51	0.02	0.24	0.03
LM_{III}	1456–1884	0.85	0.85	0.33	0.25	0.14	0.01
LM_{IV}	1884–2313	1.00	0.79	0.23	0.91	0.19	0.01
LM_V	2313–2741	0.96	0.73	0.46	0.78	0.38	0.21
D″	2741–2891	0.40	0.15	0.20	0.31	0.11	0.14

As an additional measure of robustness, we quantified the constraint provided by the data for each target parameter, as given by D_{KL} in bits. This measure of information content, or gain, indicates that the six seismic parameters in the five lower mantle layers are well-resolved ($D_{KL} > 3.7$ bits), except for η in the shallowest layer (LM_I), which is moderately constrained ($D_{KL} = 1.3$ bits, Table A.1). The data provide less constraint on the radial averages in the D″ region, which is likely related to the relatively low thickness (~150 km) compared to the other lower mantle layers (~430 km). Alternatively, the weak constraint on D″ may relate to the nature of the toroidal modes used. While the spheroidal mode data contain Stoneley modes that are primarily sensitive to this region, the toroidal mode data do not. Thus, the joint data set may not provide the complementary sensitivity to the D″ region that is required to constrain the anisotropic parameters in this part of the model.

The 1-σ predictions for *PREM* and the information gain indicate that network training was successful and that we can apply the MDNs to the observed normal mode data (Fig. 1). The most prominent feature is the small, yet robust, η anisotropy in the deeper layers (below ~1900 km). Our observation agrees with Montagner and Kennett (1996), who found negative anisotropy ($\eta < 1$) below ~2000 km, with a maximum amplitude of 1.5–2.0%, jumping to a positive anisotropy in the D″ region. However, these authors thought the lower mantle anisotropy to be insignificant, due to its relatively low amplitude and a lack of uncertainty analysis. This highlights the advantage of our Bayesian approach, which allowed us to assess the significance of the observed anisotropy. The probability of negative anisotropy in the two layers between 1884 and 2741 km is very high ($\geq$0.96) and the most probable values (the peaks of the two marginals) correspond to 0.9–1.0% of negative anisotropy (Table 1). The probability that this anisotropy is stronger than 0.5% is 0.91 (1884–2313 km) and 0.78 (2313–2741 km). This is, to our knowledge, the first robust observation of anisotropy in this part of the mantle and contrasts with the consensus that the lower mantle is isotropic. We obtained a similar result using an older spheroidal mode data set, available from the *REM* web pages (the same source as the toroidal mode data). This indicates that this information was already available in the old data, but could simply not be extracted due to the scaling and regularisation employed in previous (linear) inversions.

We further found a preference for negative, albeit very weak, P-wave anisotropy ($\phi < 1$), with probability around 0.8 throughout most of the lower mantle (Fig. 1). No significant shear-wave

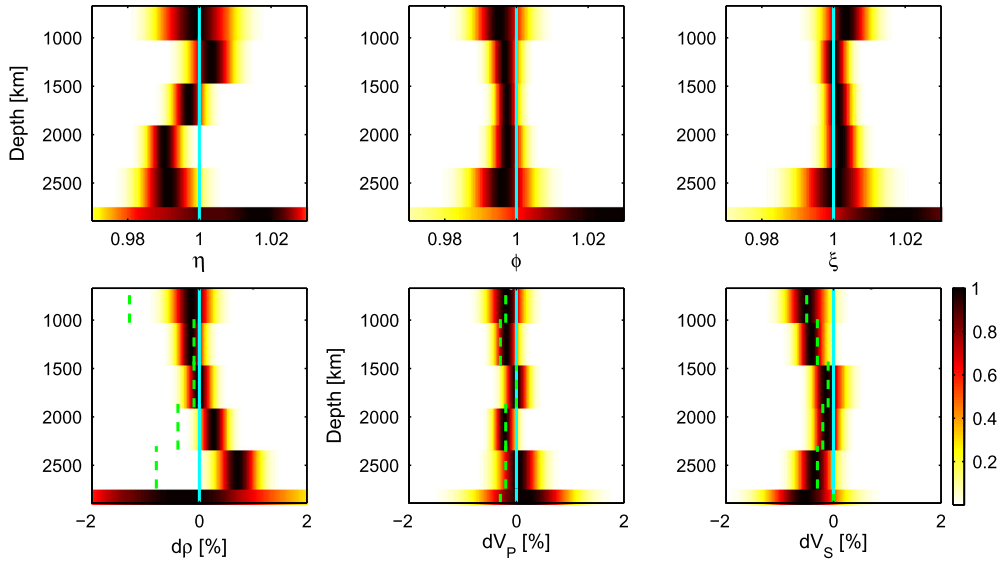

Fig. 1. 1-D marginal posterior pdfs for the averages of the six seismic parameters in the six lower mantle layers (Section 2). The bottom layer in each panel represents the D″ region. *PREM* (cyan line) is isotropic in the lower mantle and is given as a reference. The velocities and density are expressed as percentage deviations from *PREM*, as is the model *ak135f* (Kennett et al., 1995; Montagner and Kennett, 1996, green-dashed line). The probability for each 1-D pdf is rescaled so that the maximum equals 1. Asymmetric 1σ (dark colours) and 2σ (light colours from orange) error bars correspond to the $1/e^{1/2}$ (0.61) and $1/e^{2}$ (0.14) contours, respectively. (For interpretation of the references to colour in this figure legend, the reader is referred to the web version of this article.)

anisotropy (ξ) was observed, in agreement with previous studies, and Montagner and Kennett (1996), who inferred anisotropy in η, as we do here, but not in the parameters ϕ and ξ in the lower mantle. Furthermore, we found a clear positive density anomaly in the two layers below ∼1900 km: the peaks of the marginals indicate densities 0.3% and 0.7% higher than in *PREM*. This supports an earlier hypothesis (Kellogg et al., 1999) that an average excess density exists in the bottom ∼500–1000 km of the mantle, which could not unambiguously be determined in earlier studies (Masters and Gubbins, 2003; de Wit et al., 2014). The average isotropic V_S and V_P are well-constrained in the lower mantle. V_S, and in some layers V_P, deviate from *PREM*, matching the 1-D reference model *ak135* (Kennett et al., 1995) very closely. Since *ak135* was constructed using body-wave travel time measurements only, we conclude that our results for the isotropic P- and S-wave velocities are compatible with both normal mode and travel time data.

5.2. Constraints on thermochemical structure

An isotropic lower mantle has been the underlying assumption of most models of Earth's composition and dynamics. If, by contrast, the lower mantle is slightly anisotropic, it is important to understand what could be the underlying cause of this anisotropy. It could be due to SPO, in which case our seismic observations would correspond to apparent anisotropy, e.g. Fichtner et al. (2013), or LPO, which requires a mechanism of crystal alignment on a large scale. Such a mechanism is usually thought to be dislocation creep, e.g. Karato (2008). More recently, other high pressure deformation mechanisms have been suggested (Cordier et al., 2012, 2014); it needs to be investigated whether those may be important to explain anisotropy in the lower mantle.

As a starting point, we investigated whether our observed elasticity could be explained by a simple lower mantle model, given the currently available estimates of elasticity derived from mineral physics. We restricted our analysis to a polycrystal aggregate of iron-bearing perovskite and ferropericlase (Appendix B). Laboratory and first-principles modelling studies show that both minerals are anisotropic under lower mantle conditions (Karki et al., 1997, 2000; Oganov et al., 2001; Wentzcovitch et al., 2004). We varied the fractions of perovskite (X_{Pv}) and iron (X_{Fe}), the iron partitioning coefficient (K_D) and the temperature and considered all possible combinations of these parameters (Table B.2), resulting in a total of 22 491 different thermochemical models. We then rotated both minerals individually and imposed radial anisotropy, or vertical transverse isotropy, on the resulting polycrystal (Walker and Wookey, 2012). The corresponding elasticity tensor is hexagonally symmetric and it is straightforward to extract η, ϕ, ξ, ρ, V_P and V_S (Mainprice, 2007). We compared these six parameters with the (asymmetric) 2σ error levels in the six marginals for each of the five layers in the lower mantle (Fig. 1). Whenever one of the six parameters for the polycrystal aggregate lay outside the $\pm 2\sigma$ range, the corresponding thermochemical model was discarded.

The main observation is that we can find thermochemical models, and associated crystal orientations, that fit all seismic observations simultaneously. We found a strong constraint on the composition and the temperature (Fig. 2), which are mainly determined by the isotropic velocities and density. Perovskite content is primarily sensitive to V_P structure (Deschamps et al., 2007), which we observed to be similar to *PREM* (Fig. 1). For all five layers the perovskite content has to be lower than ∼75%, in agreement with Deschamps and Trampert (2004), Verhoeven et al. (2009), who used *PREM* velocities, but contradicting piclogitic models of the lower mantle, which have ∼90% perovskite (Murakami et al., 2012). The iron content is higher than 10% in all layers and increases with depth: in the deepest layer the range of accepted X_{Fe} is 14–19%. This is due to the elevated density in the deep lower mantle (Fig. 1) and explains the difference with Deschamps and Trampert (2004), Verhoeven et al. (2009), who used the density of *PREM*. In the top four layers, all accepted thermochemical models have temperatures similar to or up to 200 K lower than the Brown–Shankland geotherm (Brown and Shankland, 1981) (Fig. 2).

The required rotations of the perovskite and ferropericlase crystals, which are mainly constrained by the anisotropic parameters, indicate a tight constraint on the preferred orientation of the orthorhombic perovskite crystal (Fig. 3). Independent of depth, the perovskite crystal needs to be rotated about the two horizontal principal axes (x_1 and x_2) by approximately 30–40 degrees to match the marginals inferred for η, ϕ and ξ. There is more freedom in the rotation of the ferropericlase crystal, due to its higher degree of symmetry (cubic) compared to that of perovskite (or-

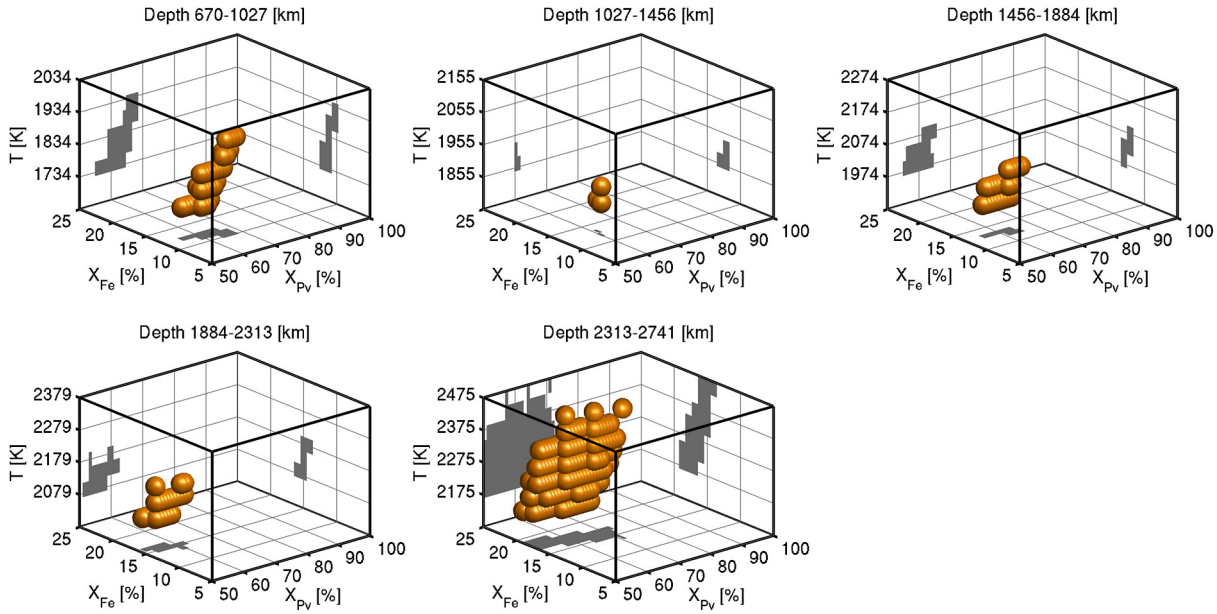

Fig. 2. Constraints on perovskite content (X_{Pv}), iron content (X_{Fe}) and temperature (T) for $K_D = 0.3$ (Table B.2). The thermochemical models that fit all six seismic parameters (η, ϕ, ξ, ρ, V_P and V_S) within their uncertainties are shown in Dutch-orange spheres (voxels) and projected in grey. The five boxes represent the five lower mantle layers, with the corresponding depth range given above each box. (For interpretation of the references to colour in this figure legend, the reader is referred to the web version of this article.)

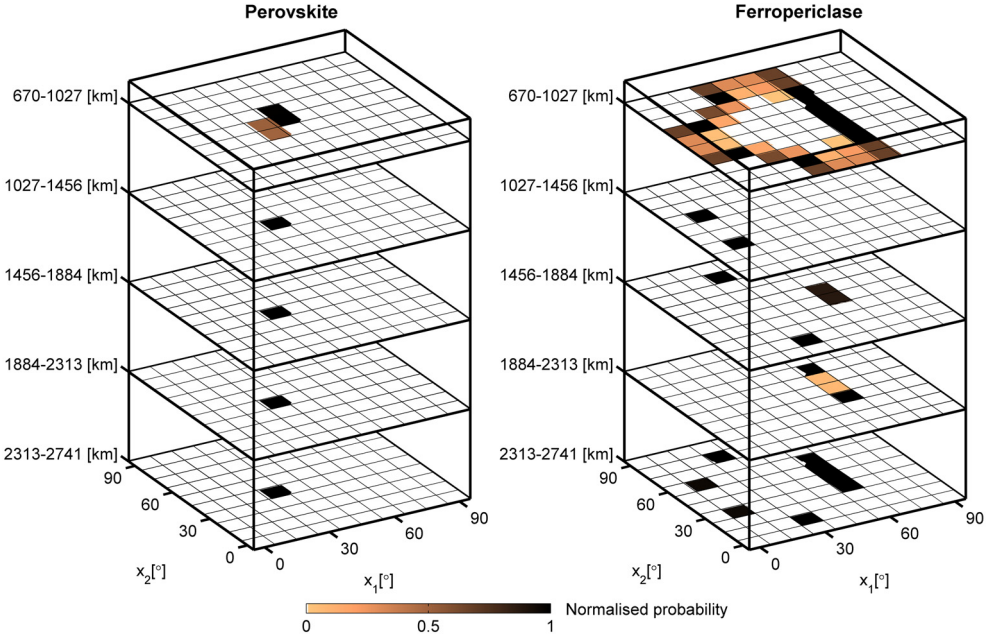

Fig. 3. Constraints on the orientation of the perovskite and ferropericlase crystals, represented by 2-D histograms of rotation angles for all accepted thermochemical models in the five lower mantle layers. In each panel, the rotation angle about two principal (horizontal) axes of the elastic tensors (x_1 and x_2) is shown for the orthorhombic perovskite (left) and cubic ferropericlase (right). The order of rotation was $x_2 - x_1(-x_3)$, where x_3 represents the vertical axis, over which we averaged to impose radial anisotropy (Appendix B). Each of the ten 2-D histograms is normalised, so that the colour indicates the relative number of accepted rotations. Empty cells represent rotation angles for which none of the 22 491 thermochemical models fits all six seismic parameters within their uncertainties.

thorhombic). An interesting observation is the difference between the accepted rotation angles for the two minerals. To explain the observed seismic anisotropy, the two minerals have to be rotated individually, i.e. about different angles, prior to the construction of the polycrystal aggregate. Our anisotropy cannot be explained by first forming a polycrystal and then rotating it, for reasons to be explored. For ease of comparison, we also visualised the accepted orientations using the more conventional Bunge Euler angles (Bunge, 1982, Supplementary Figures B.6 and B.7).

6. Discussion

Our method produces marginal distributions for individual model parameters and does not output a complete earth model, which could be used to calculate the overall fit to the data. In fact, at no point are data misfits involved in the inference process, since we sample from the prior model space. Therefore, it is instructive to conduct a simple misfit-based analysis to verify that the inferred η anisotropy in the lower mantle is indeed more com-

patible with the centre frequency measurements than an isotropic lower mantle. We considered *PREM* and set its isotropic lower mantle structure for η to the most likely values, i.e. the peaks of the marginals, for η in our five lower mantle layers. We used an L_2-norm to calculate the data misfit $\psi(\mathbf{m})$ for a given earth model $\mathbf{m}$ as

$$\psi(\mathbf{m}) = \sum_{i=1}^{N} \frac{(d_i - d_i^{syn}(\mathbf{m}))^2}{\sigma_i^2}, \tag{5}$$

where d_i is one of the N measured spheroidal and toroidal centre frequencies, $d_i^{syn}(\mathbf{m})$ is the synthetic centre frequency computed for an earth model $\mathbf{m}$ and σ_i is the corresponding estimate of measurement uncertainty. We found that the misfit is ∼9% lower for the *PREM* model with the updated η structure, indicating that the data are better explained by a lower mantle that is anisotropic in η. Note that this misfit analysis forms an additional test, which is meant to verify the robustness of our results for η, and is not part of our inversion approach. We further note that the results on ϕ and ξ are equally robust, but show no significant deviations from *PREM* and therefore cannot be assessed in a similar fashion as the results for η.

We did not impose any scaling between the anisotropic parameters. We believe that the scaling used in existing studies is responsible for not detecting any lower mantle anisotropy to date. In general, using derivatives, seismic data are most sensitive to ξ; sensitivity to ϕ and η is weak and likely to be damped out in the inverse problem. Thus, scaling ϕ and η to ξ will not reveal their anisotropy given that ξ shows no sign of anisotropy. Our method is fully non-linear, involves no derivatives and is very sensitive to complicated non-linear and weak relationships. As an experiment, we resampled our 1-D marginals for ξ to obtain the corresponding scaled versions of ϕ and η, using the scaling relations commonly used in the literature (Montagner and Anderson, 1989; Panning and Romanowicz, 2006). We illustrate this exercise for the fourth layer (1884–2313 km, Supplementary Figure A.4). The input marginal for ξ is slightly centred to the right of 1 (Fig. 1); since the assumed scaling factors are negative, we find scaled marginals slightly centred to the left of 1 for ϕ and η, the widths reflecting the values of the scaling factors. Our inferred marginals for ϕ and η are significantly different (Supplementary Figure A.4), suggesting that our data are not compatible with the scaling factors used in the literature. Similar results apply for other layers, with the peaks of the marginals at different positions, suggesting further that the data are incompatible with a single scaling factor for the whole lower mantle.

In any study based on the sampling of a model space, one has to investigate the number of samples that is necessary to successfully draw inferences on the model in question. In our experience, MDN output is conservative (pdfs are relatively wide) for a given number of samples (not shown here, see for instance de Wit et al. (2014)). Recently, Käufl et al. (2015) made a more thorough analysis of this important issue. These authors find that the posterior uncertainties output by the MDN, obtained using prior sampling, can be considered conservative estimates of the uncertainties that are obtained by directly sampling from the posterior distribution using Monte Carlo methods. This is a desirable property, since we want to minimise the possibility that a relatively narrow pdf rejects the true Earth as a possible explanation for the observations. In that sense, the MDN ensemble output reflects both the uncertainty in the earth model parameter and, to first order, the uncertainty in the inverse mapping approximated by the neural networks.

In this study, we only considered 1-D marginal posterior pdfs, which reflect our knowledge of a single model parameter, given the data and arbitrary values for all other model parameters. As such, they do not contain information on higher-dimensional structures in the posterior model space, such as trade-offs between the parameters. However, we emphasise that this does not mean that any existing trade-offs are not accounted for. All model parameters, such as velocity, density and anisotropic parameters are independently varied and no fixed scaling relations are imposed between parameters (Section 2). Any trade-offs in the full model space will cause the 1-D marginals to be wider and thus conservative, reflecting the increased uncertainty due to the existence of trade-offs.

An important question is what the interpretation of our observation could be. The normal mode data prefer an average earth model with no significant ϕ- and ξ-, but a slightly negative η-anisotropy. From an elastic tensor point of view, this puts a clear constraint on $C_{13} = C_{23}$, while $C_{11} = C_{22} = C_{33}$, $C_{44} = C_{55} = C_{66}$ and $C_{12} = C_{11} - 2C_{66}$. To explain our observations, the Earth should thus consist material that on average exhibits these properties. η also has a connection with the incidence angles of phase velocities of P- and S-waves (Dziewoński and Anderson, 1981). In future studies, body-wave wavefront studies could thus constrain the anisotropy in the lower mantle in more detail than normal mode average-frequency shifts. This idea is also explored by Kawakatsu et al. (in press).

Of course, we cannot hope to fully understand the geodynamic implications of lower mantle anisotropy from a 1-D radial model, and an extension to the 3-D case is required. However, since the strongest anisotropy is in η, and not in the parameter ξ usually investigated, it is instructive to see that existing mineral physics data are compatible with such an observation (Section 5.2). Furthermore, our simple polycrystal model implicitly assumes that all perovskite and ferropericlase crystals in the lower mantle are aligned by some mechanism. This corresponds to strong crystallographic texturing and may of course not be representative of the situation in the Earth's interior. We emphasise that we only intended to perform a first-order analysis which should be seen as a proof of concept. The simple thermochemical lower mantle model we inferred, and the associated preferred crystal orientation, merely provide a possible explanation for our seismic observations amongst maybe others.

7. Conclusion

We developed a novel Bayesian machine learning technique, to readdress the inference problem for seismic anisotropy in the lower mantle. We showed that normal mode centre frequencies can constrain radially averaged η, ϕ, ξ, ρ and the Voigt average isotropic V_P and V_S in six lower mantle layers. The results are given in terms of 1-D marginal pdfs, which allow us to quantitatively assess the probability of the observed anisotropy. The widths of the pdfs reflect uncertainty due to the implicit variation of other parameters, data uncertainty, chosen layer thickness, and the prior sampling. The results are comparable to a Backus–Gilbert inference with hard bounds, while the underlying earth models used for network training vary on a much finer scale.

We showed, for the first time, that the average lower mantle is anisotropic below 1900 km depth. This robust observation of seismic anisotropy challenges the consensus that the bulk of the lower mantle is isotropic. In addition, the mass density shows a well-constrained positive deviation from existing models at the same depths. The 1-D marginals for V_S and V_P match *ak135* closely. Since *ak135* was constructed using body-wave travel time data, we conclude that our inferences for the isotropic P-wave and S-wave velocities are compatible with both normal mode and travel time data.

We further showed that our results of lower mantle elasticity can constrain the composition, temperature and the preferred orientation of mantle-forming crystals. Given the currently available

mineral physics data, we showed that the observed anisotropy can be the result of LPO. Further investigations need to establish if SPO can be excluded, and if so, a precise mechanism at lower mantle temperature and pressure needs to be found. Only then can seismic anisotropy put constraints on the flow in the deep mantle. Furthermore, a meaningful geodynamic interpretations can only be made in a fully 3-D analysis.

Acknowledgements

We thank two anonymous reviewers for constructive reviews. We are grateful to Hanneke Paulssen for comments on an early draft of the manuscript. We thank all people who made their normal mode measurements available in various publications and on the REM webpages, and thank Paula Koelemeijer for providing additional normal mode data. Ralph de Wit is funded by the Netherlands Organisation for Scientific Research (NWO) under the grant ALW Top-subsidy 854.10.002. Computational resources for this work were provided by the Netherlands Research Center for Integrated Solid Earth Science (ISES 3.2.5 High End Scientific Computation Resources). James Wookey and Andrew Walker developed the *MSAT* toolbox used to handle elastic tensors.

Appendix A. Supplementary material

Supplementary material related to this article can be found online at http://dx.doi.org/10.1016/j.epsl.2015.07.057.

References

Babuska, V., Cara, M., 1991. Seismic Anisotropy in the Earth, vol. 10. Springer.
Backus, G.E., 1962. Long-wave elastic anisotropy produced by horizontal layering. J. Geophys. Res. 67 (11), 4427–4440.
Backus, G.E., Gilbert, F., 1968. The resolving power of gross Earth data. Geophys. J. R. Astron. Soc. 16, 169–205.
Backus, G.E., Gilbert, F., 1970. Uniqueness in the inversion of inaccurate gross Earth data. Philos. Trans. R. Soc. Lond. 266, 123–192.
Beghein, C., Trampert, J., 2003. Robust normal mode constraints on inner-core anisotropy from model space search. Science 299 (5606), 552–555.
Beghein, C., Trampert, J., van Heijst, H.J., 2006. Radial anisotropy in seismic reference models of the mantle. J. Geophys. Res. 111, B02303.
Bishop, C.M., 1995. Neural Networks for Pattern Recognition. Oxford University Press, New York.
Bozdağ, E., Trampert, J., 2008. On crustal corrections in surface wave tomography. Geophys. J. Int. 172 (3), 1066–1082.
Brown, J.M., Shankland, T.J., 1981. Thermodynamic parameters in the Earth as determined from seismic profiles. Geophys. J. Int. 66 (3), 579–596.
Bunge, H.J., 1982. Texture Analysis in Materials Science: Mathematical Methods. Butterworth's, London.
Cammarano, F., Tackley, P., Boschi, L., 2011. Seismic, petrological and geodynamical constraints on thermal and compositional structure of the upper mantle: global thermo-chemical models. Geophys. J. Int. 187, 1301–1318.
Chambat, F., Valette, B., 2001. Mean radius, mass and inertia for reference Earth's models. Phys. Earth Planet. Inter. 124, 237–253.
Chang, S.-J., Ferreira, A.M., Ritsema, J., van Heijst, H.J., Woodhouse, J.H., 2014. Global radially anisotropic mantle structure from multiple datasets: a review, current challenges, and outlook. Tectonophysics 617, 1–19.
Cobden, L., Goes, S., Ravenna, M., Styles, E., Cammarano, F., Gallagher, K., Connolly, J.A.D., 2009. Thermochemical interpretation of 1-D seismic data for the lower mantle: the significance of nonadiabatic thermal gradients and compositional heterogeneity. J. Geophys. Res., Solid Earth 114 (B11).
Cordier, P., Amodeo, J., Carrez, P., 2012. Modelling the rheology of MgO under Earth's mantle pressure, temperature and strain rates. Nature 481, 177–180.
Cordier, P., Demouchy, S., Beausir, B., Taupin, V., Barou, F., Fressengeas, C., 2014. Disclinations provide the missing mechanism for deforming olivine-rich rocks in the mantle. Nature 507, 51–56.
Dahlen, F., Tromp, J., 1998. Theoretical Global Seismology. Princeton University Press.
de Wit, R.W.L., Trampert, J., van der Hilst, R.D., 2012. Toward quantifying uncertainty in travel time tomography using the null-space shuttle. J. Geophys. Res. 117, B03301.
de Wit, R.W.L., Valentine, A.P., Trampert, J., 2013. Bayesian inference of Earth's radial seismic structure from body-wave traveltimes using neural networks. Geophys. J. Int. 195, 408–422.
de Wit, R.W.L., Käufl, P.J., Valentine, A.P., Trampert, J., 2014. Bayesian inversion of free oscillations for Earth's radial (an)elastic structure. Phys. Earth Planet. Inter. http://dx.doi.org/10.1016/j.pepi.2014.09.004.
Deschamps, F., Trampert, J., 2004. Towards a lower mantle reference temperature and composition. Earth Planet. Sci. Lett. 222 (1), 161–175.
Deschamps, F., Trampert, J., Tackley, P.J., 2007. Thermo-chemical structure of the lower mantle: seismological evidence and consequences for geodynamics. In: Yuen, D., Maruyama, S., Karato, S.-I., Windley, B. (Eds.), Superplumes: Beyond Plate Tectonics. Springer, Netherlands, pp. 293–320.
Deuss, A., Ritsema, J., van Heijst, H., 2013. A new catalogue of normal-mode splitting function measurements up to 10 mHz. Geophys. J. Int. 193 (2), 920–937.
Dziewoński, A.M., Anderson, D.L., 1981. Preliminary reference Earth model. Phys. Earth Planet. Inter. 25, 297–356.
Fichtner, A., Kennett, B.L., Trampert, J., 2013. Separating intrinsic and apparent anisotropy. Phys. Earth Planet. Inter. 219, 11–20.
Karato, S.-I., 2008. Deformation of Earth Materials: An Introduction to the Rheology of Solid Earth. Cambridge University Press, Cambridge, UK.
Karato, S.-I., Zhang, S., Wenk, H.-R., 1995. Superplasticity in Earth's lower mantle: evidence from seismic anisotropy and rock physics. Science 270 (5235), 458–461.
Karki, B., Stixrude, L., Clark, S., Warren, M., Ackland, G., Crain, J., 1997. Elastic properties of orthorhombic $MgSiO_3$ perovskite at lower mantle pressures. Am. Mineral. 82 (5), 635–638.
Karki, B.B., Wentzcovitch, R.M., de Gironcoli, S., Baroni, S., 2000. High-pressure lattice dynamics and thermoelasticity of MgO. Phys. Rev. B 61, 8793–8800.
Käufl, P.J., Valentine, A.P., O'Toole, T.B., Trampert, J., 2014. A framework for fast probabilistic centroid-moment-tensor determination — inversion of regional static displacement measurements. Geophys. J. Int. 196 (3), 1676–1693.
Käufl, P.J., Valentine, A.P., de Wit, R.W.L., Trampert, J., 2015. Robust and fast probabilistic source parameter estimation from near-field displacement waveforms using pattern recognition. Bull. Seismol. Soc. Am. 105 (4), 2299. http://dx.doi.org/10.1785/0120150010.
Kawakatsu, H., Montagner, J.-P., Song, T.-R.A., in press. On DLA's η. In: Foulger, J.E.A. (Ed.), GSA Special Paper 514: The Interdisciplinary Earth: A volume in honour of Don L. Anderson. Geol. Soc. Am.. http://www.mantleplumes.org/TopPages/TheDLABook.html.
Kellogg, L.H., Hager, B.H., van der Hilst, R.D., 1999. Compositional stratification in the deep mantle. Science 283 (5409), 1881–1884.
Kennett, B., 2006. On seismological reference models and the perceived nature of heterogeneity. Phys. Earth Planet. Inter. 159, 129–139.
Kennett, B., Engdahl, E.R., Buland, R., 1995. Constraints on seismic velocities in the Earth from travel times. Geophys. J. Int. 122, 108–124.
Koelemeijer, P.J., 2014. Normal mode studies of long wavelength structures in Earth's lowermost mantle. Ph.D. thesis. University of Cambridge, Cambridge, UK.
Koelemeijer, P., Deuss, A., Ritsema, J., 2013. Observations of core–mantle boundary Stoneley modes. Geophys. Res. Lett. 40 (11), 2557–2561.
Kustowski, B., Ekström, G., Dziewoński, A.M., 2008. Anisotropic shear-wave velocity structure of the Earth's mantle: a global model. J. Geophys. Res., Solid Earth 113 (B6).
Love, A.E.H., 1927. A Treatise on the Mathematical Theory of Elasticity. Cambridge University Press, New York.
MacKay, D., 2003. Information Theory, Inference, and Learning Algorithms. Cambridge Univ. Press.
Mainprice, D., 2007. 2.16 – seismic anisotropy of the deep earth from a mineral and rock physics perspective. In: Schubert, G. (Ed.), Treatise on Geophysics. Elsevier, Amsterdam, pp. 437–491.
Mainprice, D., Barruol, G., Ben Ismaïl, W., 2000. The anisotropy of the Earth's mantle: from single crystal to polycrystal. In: Karato, S.I., Forte, A.M., Liebermann, R.C., Masters, G., Stixrude, L. (Eds.), Earth's Deep Interior. Mineral Physics and Tomography from the Atomic to the Global Scale. In: Geophysical Monograph Series, vol. 117. AGU, Washington, D.C., pp. 237–264.
Masters, G., Gubbins, D., 2003. On the resolution of density within the Earth. Phys. Earth Planet. Inter. 140, 159–167.
Masters, G., Barmine, M., Kientz, S., 2011. Mineos: User Manual Version 1.0.2. Calif. Inst. of Tech., Pasadena, CA.
McNamara, A.K., van Keken, P.E., Karato, S.-I., 2002. Development of anisotropic structure in the Earth's lower mantle by solid-state convection. Nature 416 (6878), 310–314.
Meade, C., Silver, P.G., Kaneshima, S., 1995. Laboratory and seismological observations of lower mantle isotropy. Geophys. Res. Lett. 22 (10), 1293–1296.
Meier, U., Curtis, A., Trampert, J., 2007. Global crustal thickness from neural network inversion of surface wave data. Geophys. J. Int. 169, 706–722.
Møller, M.F., 1993. A scaled conjugate gradient algorithm for fast supervised learning. Neural Netw. 6, 525–533.
Montagner, J.-P., 1994. Can seismology tell us anything about convection in the mantle? Rev. Geophys. 32 (2), 115–137.
Montagner, J.-P., Anderson, D.L., 1989. Petrological constraints on seismic anisotropy. Phys. Earth Planet. Inter. 54 (1–2), 82–105.
Montagner, J.-P., Kennett, B.L.N., 1996. How to reconcile body-wave and normal-mode reference earth models. Geophys. J. Int. 125, 229–248.

Murakami, M., Ohishi, Y., Hirao, N., Hirose, K., 2012. A perovskitic lower mantle inferred from high-pressure, high-temperature sound velocity data. Nature 485 (7396), 90–94.

Nowacki, A., Wookey, J., Kendall, J.-M., 2011. New advances in using seismic anisotropy, mineral physics and geodynamics to understand deformation in the lowermost mantle. J. Geodyn. 52 (3–4), 205–228.

Oganov, A.R., Brodholt, J.P., Price, G.D., 2001. The elastic constants of $MgSiO_3$ perovskite at pressures and temperatures of the Earth's mantle. Nature 411, 934–937.

Panning, M., Romanowicz, B., 2004. Inference on flow at the base of Earth's mantle based on seismic anisotropy. Science 303, 351–353.

Panning, M., Romanowicz, B., 2006. A three-dimensional radially anisotropic model of shear velocity in the whole mantle. Geophys. J. Int. 167 (1), 361–379.

Panning, M., Lekić, V., Romanowicz, B., 2010. Importance of crustal corrections in the development of a new global model of radial anisotropy. J. Geophys. Res., Solid Earth 115 (B12).

Reference Earth Model web pages, 2001. http://igppweb.ucsd.edu/~gabi/rem.dir/surface/tmodes.list.

Tarantola, A., 2005. Inverse Problem Theory and Methods for Model Parameter Estimation. SIAM.

Tarantola, A., Valette, B., 1982. Inverse Problems = Quest for Information. J. Geophys. 50, 159–170.

Verhoeven, O., Mocquet, A., Vacher, P., Rivoldini, A., Menvielle, M., Arrial, P.-A., Choblet, G., Tarits, P., Dehant, V., Van Hoolst, T., 2009. Constraints on thermal state and composition of the Earth's lower mantle from electromagnetic impedances and seismic data. J. Geophys. Res., Solid Earth 114 (B3).

Visser, K., Trampert, J., Lebedev, S., Kennett, B., 2008. Probability of radial anisotropy in the deep mantle. Earth Planet. Sci. Lett. 270 (3–4), 241–250.

Walker, A.M., Wookey, J., 2012. Msat: new toolkit for the analysis of elastic and seismic anisotropy. Comput. Geosci. 49 (0), 81–90.

Wentzcovitch, R.M., Karki, B.B., Cococcioni, M., de Gironcoli, S., 2004. Thermoelastic properties of $MgSiO_3$-perovskite: insights on the nature of the Earth's lower mantle. Phys. Rev. Lett. 92, 018501.

Widmer, R., 1991. The large-scale structure of the deep Earth as constrained by free oscillation observations. Ph.D. thesis. University of California, San Diego, CA, USA.

Woodhouse, J., Giardini, D., 1985. Inversion for the splitting function of isolated low order normal mode multiplets. EOS, Trans. Am. Geophys. Union 66, 300.